*applied sciences*

MDPI

*Article*

# Active Push-Assisted Yaw-Correction Control for Bridge-Area Vessels via ESO and Fuzzy PID

**Cheng Fan [1], Xiongjun He [1], Liwen Huang [2,3], Teng Wen [2,3] and Yuhong Zhao [2,3,*]**

[1] School of Transportation and Logistics Engineering, Wuhan University of Technology, Wuhan 430063, China; 15807128239@163.com (C.F.); hxjwhut@163.com (X.H.)
[2] Hubei Key Laboratory of Inland Shipping Technology, Wuhan 430063, China; lwhuang@whut.edu.cn (L.H.); 346232@whut.edu.cn (T.W.)
[3] School of Navigation, Wuhan University of Technology, Wuhan 430063, China
* Correspondence: 360746@whut.edu.cn

**Abstract**

This paper investigates ship–pier collision risk caused by yaw deviation in inland bridge waterways. The proposed framework is conceived for fixed auxiliary thruster installation in bridge areas, rather than retrofitting shipboard propulsion systems. A proactive intervention scheme is developed based on state estimation and short-horizon prediction. A Kalman filter is used for state fusion and short-horizon motion prediction. Yaw events are detected via a threshold rule with consecutive-decision logic. An extended state observer (ESO) is adopted to estimate lumped disturbances and model uncertainties. A fuzzy self-tuning PID law is then applied to generate thruster commands for closed-loop corrective control. Numerical simulations suggest that, relative to rudder-only recovery, thruster-assisted intervention yields improved restoration behavior, reduced lateral deviation accumulation, and increased minimum clearance to bridge piers under the tested conditions. Additional tests with cross-current disturbances indicate that the risk-triggered scheme with ESO-based compensation can maintain stable recovery and a higher safety margin. The proposed approach provides an engineering-oriented pathway to extend bridge-area risk management from warning-level assessment to executable control intervention.

**Keywords:** inland bridge waterways; ship yaw deviation; thruster-assisted corrective control; active intervention; ESO-based fuzzy self-tuning PID

## 1. Introduction

With increasing shipping demand and an increasing number of bridges spanning navigable waterways, exposure to ship–bridge collisions has increased and remains a sustained concern [1–3]. Statistical studies on bridge failures indicate that ship impact is an important external cause of bridge failure [4,5]. Ship–bridge collisions are relatively low-frequency events worldwide. However, they often lead to severe consequences. PIANC statistics reported 35 major bridge collapses caused by ship or barge impacts during 1960–2015, with substantial loss of life [6]. The 2024 bridge-collapse accident in Baltimore, United States, further highlighted the systemic impact of such events on transport networks and urban safety [7].

At present, ship–bridge collision prevention systems are generally categorized into passive protection and active protection [8]. Passive protection mainly relies on static structures, such as pier protection, fenders, protective dolphins, and guiding/deflecting structures, to mitigate collision effects through energy absorption and force redistribution.

Check for updates

Academic Editor: José A. Orosa García

Received: 27 January 2026
Revised: 2 March 2026
Accepted: 3 March 2026
Published: 5 March 2026

**Copyright:** © 2026 by the authors. Licensee MDPI, Basel, Switzerland. This article is an open access article distributed under the terms and conditions of the Creative Commons Attribution (CC BY) license.

Recent studies have focused on improving energy-absorption efficiency, reducing peak impact force, and enhancing repairability. For example, steel pipe pile cofferdams filled with sand dissipate energy via friction and sand-particle crushing, thereby improving impact resistance [9]. Trapezoidal corrugated plate–aluminum foam composite sandwich devices can reduce peak collision force and prolong the impact duration [10,11]. Passive protection offers clear advantages in reliability and cost control, but it functions primarily as post-contact loss mitigation and thus provides limited capability for pre-contact correction of heading or lateral deviation under sudden off-course events, loss of control, or strong current and crosswind disturbances.

Active protection emphasizes reducing accident probability and primarily relies on multi-source sensing, early warning, and traffic management in bridge areas. In China, an engineering-oriented specification system has been established. The *Technical Specification for Application of Highway Bridge Anti-Ship-Collision Early Warning Systems* defines requirements for system components and application. Research in this area focuses on sensor fusion and risk identification. An intelligent warning configuration based on yaw-deviation monitoring can provide risk alerts and support management actions [12]. Radar–AIS–video fusion enhances target recognition, but it may suffer from radar clutter and AIS occlusion in complex bridge environments [13]. Trajectory prediction methods that fuse AIS and radar via Kalman filtering enable real-time detection of high-risk behaviors, such as course deviation and overspeeding, and can trigger timely warnings [14].

International studies generally follow two lines: bridge-area-level risk assessment and ship-level situational awareness. Bridge-area-level studies emphasize historical databases and probabilistic models. They support site selection, traffic management, and design verification of protective facilities [15]. Platforms such as BOPVis support integrated visualization of bridge monitoring and navigational information [16]. The AASHTO framework provides risk assessment and design procedures and has been widely applied [17]. Some studies further incorporate ship impact into life-cycle performance–cost–decision frameworks [18]. Ship-level studies focus on near-real-time risk assessment and decision support for individual ships. In the IBS context, methods for detecting and quantifying collision risk have been proposed [19]. Combining AIS data with maneuvering simulation can be used to evaluate collision (allision) probability, impact energy demand, and the effectiveness of measures such as speed limits and adjustments to traffic management [20]. Pan et al. proposed a collision-probability assessment that accounts for ship-scale effects [2].

Overall, active ship–bridge collision prevention has been widely studied and implemented for monitoring, warning, and traffic control. However, the effectiveness of post-warning avoidance largely depends on human actions and the vessel's available maneuverability. Under loss of control, communication or power failures, or a short available response time, warning information may not be converted into effective corrective maneuvers in time. To enhance pre-collision risk suppression, recent studies have begun to explore bridge-area protective facilities with motion-intervention capability. Flexible guiding anti-collision devices (FGADs) can, to some extent, extend the interaction time, reduce impact force, and induce a corrective heading deflection [21]. Interception-based schemes, in contrast, trigger structural restrictions based on monitoring to prevent high-risk vessels from entering bridge areas [22]. While these studies provide valuable risk identification and warning capabilities, many intervention measures are still activated at the contact or near-contact stage or when collision becomes nearly inevitable. For inland-waterway scenarios where a vessel yaws into a hazardous region but still has a response window, it is necessary to further explore how early-warning information can be translated into timely and controllable pre-collision corrective actions. It should be noted that the proposed active-intervention framework targets the deployment of fixed push-assist devices in bridge

areas as an extension of protective infrastructure. It does not require any modification of the vessel's onboard propulsion system.

From a closed-loop perspective, pre-collision correction requires an integrated chain of risk evolution characterization, trigger boundary definition, and thrust generation and control. State estimation and short-horizon trajectory prediction provide essential foundations [23]. Given the low update rate, missing data, and noise in AIS, Kalman filtering and its variants are widely used for track smoothing and prediction, including polynomial Kalman filtering and learning-assisted next-point prediction coupled with an extended Kalman filter (EKF) [24]. Meanwhile, disturbances such as local flow fields and crosswinds in bridge areas can strongly affect heading and lateral responses; extended state observers (ESOs), which estimate and compensate for lumped disturbances online, have been applied to ship heading-keeping and unmanned surface vehicle control [25,26].

In recent years, neuro-fuzzy methods have also been used for observer design in nonlinear and uncertain systems. Related studies often use Takagi–Sugeno (TS) or quasi-linear parameter-varying (qLPV) forms to represent nonlinearities and time-varying parameters. They commonly combine learning mechanisms, such as ANFIS, to build observers. They generate residuals for fault diagnosis and fault detection and isolation (FDI). Existing work has applied TS neuro-fuzzy observers to fault diagnosis in wind turbine systems. Other studies combine neuro-fuzzy qLPV modeling with zonotope set estimation and build qLPV zonotopic observer banks for FDI [27,28]. These studies mainly emphasize estimation and diagnosis, whereas we focus on execution-level coupling from risk cues to bounded lateral-thrust correction in bridge-area scenarios with a remaining response window.

However, despite progress in risk identification and uncertainty characterization (e.g., [2,15]), coupling mechanisms that translate such risk cues into controllable lateral-thrust correction remain insufficiently documented for bridge-area scenarios with a remaining response window. Specifically, current methodologies exhibit limitations in the following three aspects:

(1) Limited prediction–control coupling: short-horizon prediction is widely used for warning generation or traffic management; however, closed-loop coupling mechanisms that convert predicted risk evolution into execution-level corrective inputs within a bounded handling window remain insufficiently articulated.
(2) Trigger boundaries weakly linked to safety margin: Intervention triggers are often defined by empirical thresholds or single risk indicators. Such definitions may not explicitly relate trigger timing to the remaining controllable safety margin, which may weaken the reliability of actionable pre-collision intervention in practice.
(3) Insufficient robust and smooth execution-level control: under environmental disturbances and model mismatch, thrust output may exhibit oscillation or excessive variation. Methods that explicitly ensure smooth and bounded thrust generation while compensating aggregated disturbances online remain insufficiently addressed in bridge-area applications.

To address these gaps, this study proposes a push-assist active correction method for high-risk yaw-deviation scenarios in inland bridge areas. Specifically, Kalman filtering provides short-horizon state estimation and prediction; the trigger boundary is tied to safety-margin-related indicators to define an actionable handling window; and ESO with a fuzzy self-tuning incremental PID enables online compensation of lumped disturbances and smooth and bounded thrust generation for execution-level correction. The framework integrates these modules into an executable chain for pre-collision correction, i.e., state estimation/prediction, safety-margin-related triggering, and disturbance-rejected thrust regulation. The method outputs controllable lateral thrust and coordinates with rudder

control. It suppresses the growth of lateral deviation within a limited handling window and increases the safety margin to bridge piers.

It should be emphasized that the Kalman filter, ESO, and fuzzy self-tuning incremental PID are established methods. This study does not claim theoretical algorithmic novelty. The contribution lies in integrating these methods into an executable closed-loop coupled framework for pre-collision correction in bridge areas. The proposed framework is validated within a modeled inland bridge-area scenario under defined disturbance conditions. It aims to provide an engineering reference for shifting bridge-area risk handling from early warning to actionable intervention.

## 2. Overall Architecture of the Intelligent Push-Assisted System

To mitigate navigation safety hazards caused by vessel yaw deviation in bridge areas, this study proposes and designs an intelligent push-assisted control system for real-time intervention. The system is built around continuous state sensing, trajectory prediction, intelligent thrust decision-making, and closed-loop feedback regulation, forming a complete control chain from yaw-deviation trend identification to thrust-intervention execution.

Unlike conventional passive response modes dominated by manual pilotage and static aids to navigation, the proposed system enables proactive, anticipatory intervention through sensing and prediction, thereby improving the timeliness and accuracy of yaw-risk handling. Its key features include: (i) early identification of potential yaw-deviation trends supported by Kalman-filter-based state estimation and trajectory prediction; (ii) intelligent thrust decisions driven by heading error and evolving environmental conditions, with real-time adaptive adjustment; and (iii) targeted, precise intervention on the subject vessel to ensure heading correction while improving the efficiency of control-resource utilization.

Based on a hierarchical prediction–decision–control architecture, the overall framework of the lateral thruster control system is established, as shown in Figure 1. In the figure, $F_{push}$ and $F$ denote the target thruster thrust and the thruster thrust acting on the target vessel, respectively; $f$ and represent the thrust error and its rate of change; $K_P$, $T_i$, and $T_d$ are the proportional gain, integral time constant, and derivative time constant of the PID controller, respectively; $\gamma$ is the disturbance-compensation coefficient matrix; and $(X_s,\ Y_s)$ denotes the current vessel position. $F_{pid}$ and $F_{rid}$ are the PID output command and the final compensated thruster-thrust command, respectively. The system comprises three functional modules—prediction, decision, and control. The prediction module forecasts the vessel's future trajectory and heading angle, while the decision module computes the required push-assisted thruster thrust based on the heading angle. The control module adopts a composite strategy that integrates ESO-based feedforward compensation with a fuzzy self-tuning PID. Specifically, the ESO provides a disturbance feedforward term for active disturbance rejection, and the fuzzy PID tunes controller parameters online according to the thrust error and its rate of change to implement feedback control, finally synthesizing the thruster-thrust command.

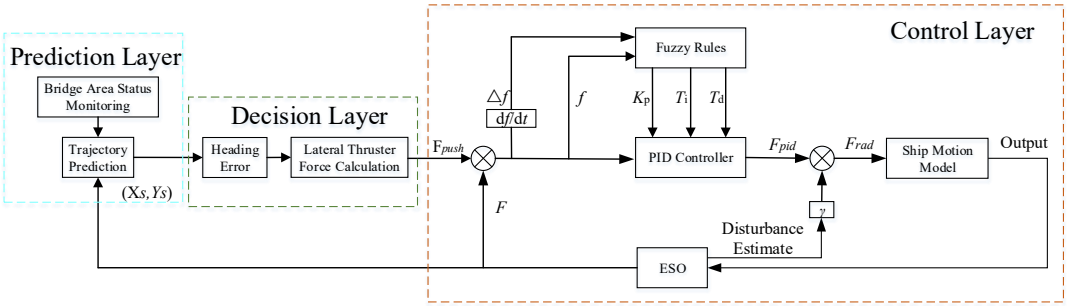



**Figure 1.** Overall lateral thruster control architecture.

## 3. Vessel State Prediction and Thruster Thrust Calculation

To meet the requirement for executable active control following bridge-area early warnings, this section establishes a workflow comprising Kalman-based state estimation and short-horizon prediction, yaw-deviation identification using thresholding and continuous discrimination, and thruster thrust calculation with target-thrust computation. The workflow provides state variables and reference inputs for subsequent closed-loop correction control based on an MMG vessel model.

### *3.1. Kalman Filter-Based State Estimation and Prediction*

To ensure navigational safety in bridge areas, the system needs real-time trajectory estimation and short-horizon prediction. This capability supports yaw-deviation identification and intervention control. However, GNSS measurement errors, sensor noise, and numerical discretization errors are unavoidable. Direct kinematic extrapolation from raw observations can lead to unstable predictions and accumulated errors. To address this issue, this study introduces a discrete Kalman filter to dynamically estimate and refine the vessel's planar position state [29]. Consider the discrete sampling instant $k$ and the sampling period $T$. In the simulations, the time step is set to $\Delta t = 0.2\,s$; thus, $T = 0.2\,s$. The initial vessel speed is set to $V = 5\,kn$. This corresponds to a per-step displacement of approximately $\Delta S \approx VT \approx 0.51\,m$. This setting captures trajectory details of yaw-deviation development in bridge areas while meeting real-time computational requirements.

This study estimates only the planar position states. The two-dimensional state vector is defined as $X(k) = [x(k), y(k)]^T$, and the measurement vector is $(k) = [Z_x(k), Z_y(k)]^T$. Under the constant course and speed (CCS) assumption [30,31], the position recursion can be expressed as

$$\begin{cases} x(k) = x(k-1) + V(k-1)T\cos(C(k-1)) \\ y(k) = y(k-1) + V(k-1)T\sec(x_m(k-1))\sin(C(k-1)) \end{cases} \quad (1)$$

where $x_m(k-1) = \frac{x(k-1)+x(k)}{2}$. By rearranging Equation (1) into a matrix form, the discrete state equation can be written as

$$X(k) = \mathbf{A}X(k-1) + \mathbf{B}i(k-1) + \mathbf{C}w(k-1) + v(k-1) \quad (2)$$

In this equation, $i(k-1)$ is the deterministic kinematic input vector constructed from the vessel speed and heading. $w(k-1)$ denotes external disturbance inputs, such as wind and current. $v(k-1)$ is the process noise term, which represents unmodeled dynamics and discretization errors. Since the state vector contains only position components, the state transition matrix is set to the identity matrix:

$$A = \begin{bmatrix} 1 & 0 \\ 0 & 1 \end{bmatrix} \quad (3)$$

The process noise is assumed to be zero-mean Gaussian white noise, i.e., $v(k) \sim N(0, Q)$. GNSS provides direct position measurements.

Therefore, the measurement equation is written as

$$Z(k) = HX(k) + \theta(k) \quad (4)$$

where $H$ is the observation matrix:

$$\mathrm{H} = \begin{bmatrix} 1 & 0 \\ 0 & 1 \end{bmatrix} \tag{5}$$

The measurement noise satisfies $\psi(k) \sim N(0, R)$ and is assumed to be independent of the process noise. In Equation (3), $A$ is the state transition matrix and describes the time evolution of the state. In Equation (4), $H$ is the observation matrix and maps the state to the measurement space. These matrices have different physical meanings.

The Kalman filter recursion follows the "predict–update" structure in Equation (6):

$$\begin{cases} \hat{x}_k^- = A\hat{x}_k + Bu_{k-1} \\ P_K^- = AP_{k-1}A^T + Q \\ K_K = P_K^- H^T (HP_K^- H^T + R)^{-1} \\ \hat{x}_k = \hat{x}_k^- + K_k(Z_k - H\hat{x}_k^-) \\ P_k = (I - K_k H)P_K^- \end{cases} \tag{6}$$

Here, $Q$ and $R$ are the covariance matrices of the process noise and the measurement noise, respectively. The specific values are taken from Ref. [32]. The measurement-noise covariance $R$ is determined by the positioning sensor accuracy. The measurement noise is modeled based on a typical planar GNSS positioning accuracy. The planar positioning standard deviation is set to $\delta_{gps}$ = 0.5 m. The measurement errors in the east–west and north–south directions are assumed to be approximately independent. Thus,

$$R = \begin{bmatrix} \delta_{gps}^2 & 0 \\ 0 & \delta_{gps}^2 \end{bmatrix} = \begin{bmatrix} 0.25 & 0 \\ 0 & 0.25 \end{bmatrix} \tag{7}$$

Process-noise covariance matrix $Q$ is used to characterize the equivalent unmodeled displacement uncertainty introduced by the straight-line motion simplification, discrete integration errors, and model mismatch during yaw/turning maneuvers. Since the state vector contains only planar position $[x, y]^T$, the process noise is modeled as an additional random displacement at each sampling step.

To ensure reproducible parameter selection, this uncertainty is parameterized by the relative fraction of the one-step displacement. Let $\Delta S \approx VT$ denote the one-step displacement and let $\delta_p$ denote the corresponding one-step displacement standard deviation.

$$\delta_p = \alpha \Delta S = \alpha VT$$

Here, $\alpha$ denotes the relative fraction of model mismatch in the one-step displacement. Under the baseline setting, $T$ = 0.2 s and $V$ = 5 kn ($\Delta S \approx 0.51$ m). We set $\alpha$ = 0.02, i.e., an equivalent uncertainty of about 2% of the one-step displacement. This gives $\delta_p \approx 0.010$ m, and thus,

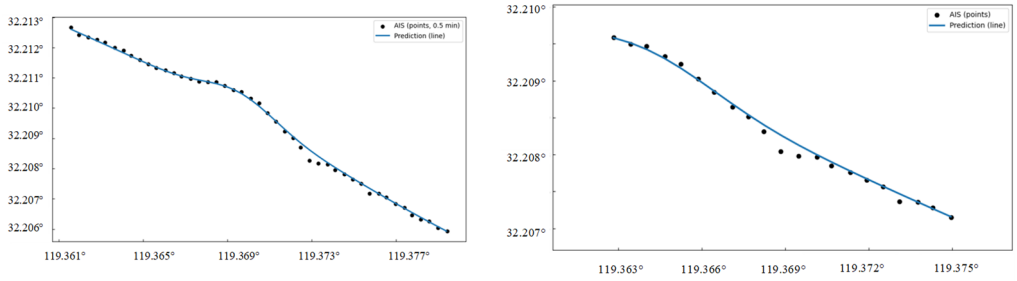
$$Q = \begin{bmatrix} 1 \times 10^{-4} & 0 \\ 0 & 1 \times 10^{-4} \end{bmatrix} \tag{8}$$

This yields $Q/R \approx 4 \times 10^{-4}$, which matches the common engineering setting $Q \ll R$. It helps the filter suppress measurement noise without relying too heavily on the simplified kinematic model. This improves the robustness of bridge-area yaw-deviation identification and short-horizon prediction.

It should be noted that, when external disturbances such as wind and current are considered, $Q$ can be increased by enlarging $\alpha$, or tuned adaptively based on innovation

statistics. In this study, the still-water baseline simulation uses the fixed small process noise in Equation (8), which is sufficient for stability and reproducibility.

Accordingly, recursive computation using Equation (2) yields a smoothed position estimate and a short-horizon predicted trajectory $(\hat{x}_{k+i|k}, \hat{y}_{k+i|k})$. Figure 2 shows an example of vessel trajectory prediction. The overall and local prediction performance satisfy the trajectory-tracking requirements in bridge areas. Minor errors may occur during turning maneuvers due to nonlinear maneuvering effects, which is expected in practice.




(**a**) Overall predicted vessel trajectory (**b**) Local predicted vessel trajectory

**Figure 2.** Predicted vessel motion trajectories.

### *3.2. Yaw Deviation Identification and Target Thrust Determination*

To identify yaw-deviation risk before the vessel approaches a bridge pier, the filtered heading estimate $\hat{\theta}$ is compared with a predefined reference heading $\theta_{ref}$ for the bridge area to compute the heading error $\Delta\theta$, as given in Equation (9):

$$\Delta\theta(k) = \hat{\theta}(k) - \theta_{ref} \tag{9}$$

Here, $\theta_{ref}$ is the reference heading defined according to the centerline direction of the navigation channel in the bridge area. To balance sensitivity and false-alarm rate, a heading-error detection threshold $\Delta\theta_{thres}$ is introduced, typically set between 3° and 5°. The specific threshold can be determined by considering factors such as channel width, traffic density, and the intensity of wind–current disturbances in the bridge area. When the heading difference satisfies Equation (10), the vessel is identified as yaw-deviated:

$$|\Delta\theta(k)| > \Delta\theta_{thres} \tag{10}$$

To improve detection accuracy, a consecutive-confirmation mechanism is introduced, requiring that Equation (10) be satisfied over several consecutive detection intervals (e.g., 2–3 cycles) to reduce false alarms caused by single-measurement errors. The yaw-deviation identification result is used as the trigger condition for thruster-thrust calculation and provides the error input for subsequent target-thrust computation.

The push-assist device provides a lateral thrust $F_{push}$. It acts on the hull with an approximately fixed lever arm $d$, generating a corrective yaw moment $M_{push} = F_{push}\boldsymbol{d}$. In short-horizon correction scenarios in bridge areas, where sudden yaw deviation occurs and the vessel approaches a bridge pier, the heading error $\Delta\theta$ should converge quickly while maintaining a consistent correction direction. Therefore, $sin(\Delta\theta)$ is used as an equivalent error term. For small deviations (on the order of a few degrees), $sin(\Delta\theta) \approx \Delta\theta$, which yields an approximately linear mapping and facilitates control design. For larger deviations, $sin(\Delta\theta)$ remains bounded. This avoids unrealistic commands caused by an unbounded thrust demand as the angle increases.

In addition, a larger vessel typically requires a higher corrective moment. This study introduces the vessel length $L$ as a scaling factor and uses $L^2$ to represent the trend of scale amplification on moment/thrust demand. Factors related to vessel hydrodynamics, the

device lever arm $d$, and unmodeled maneuvering differences are lumped into a composite correction coefficient $k$. This establishes the mapping between the target push thrust $F_{push}$ and the heading deviation, with an environmental compensation term. The mapping is given in Equation (11):

$$F_{push} = k \cdot L^2 \cdot \sin(\Delta\theta) + C_{env} \tag{11}$$

In Equation (11), $F_{push}$ denotes the lateral thruster thrust. $k$ is a composite correction coefficient reflecting the vessel's hydrodynamic characteristics. $L$ is the vessel length. $\Delta\theta$ is the current heading deviation angle. $C_{env}$ is the environmental disturbance compensation term, which corrects thrust errors under wind and current disturbances. $F_{push}$ is in N and $L$ is in m. $sin(\Delta\theta)$ is dimensionless. Therefore, $k$ has the unit of $N/m^2$, ensuring dimensional consistency of Equation (11). $C_{env}$ is also expressed in N as an equivalent thrust compensation.

For thrust modeling, the following assumptions are adopted for simplification. The lever arm $d$ of the push-assist device is treated as a constant. The effects of vessel rotational inertia and hydrodynamic coupling are equivalently lumped into the scaling term $L^2$ and under the coefficient $K$ . Under the baseline experimental conditions (still water or weak wind and current), $C_{env}$ can be neglected, i.e.,

$$F_{push} \approx k \cdot L^2 \cdot \sin(\Delta\theta) \tag{12}$$

To prevent abrupt thrust changes and actuator saturation, the target thrust is further subject to magnitude limits and directional constraints:

$$F_{push} \leftarrow sat(F_{push}, -F_{\max}, F_{\max}) \tag{13}$$

Here, $F_{max}$ denotes the maximum thrust deliverable by the push-assisted device, and $sat(\cdot)$ denotes the saturation function. The thrust direction is determined by the sign of $\Delta\theta$ (a deviation to port triggers a starboard push, whereas a deviation to starboard triggers a port push).

The composite correction coefficient $k$ is calibrated using full-scale bridge-area trial data to improve reproducibility. The calibration data come from bridge-area navigation records collected from 12:00 to 14:00 on 12 January 2026. AIS/GNSS provides position, speed, and heading, while the thruster controller/trial logs provide thruster commands (or RPM/current/power) for thrust calculation. To avoid the ambiguity that thrust cannot be obtained from AIS alone, the thruster command $u_T$ is converted into an equivalent lateral thrust $F_{test}$ (N) using the manufacturer's thrust calibration curve (or a bollard-pull calibration curve), and paired with the synchronous heading error $\Delta\theta$ to form samples. Data preprocessing includes outlier removal, heading unwrapping, and bridge-area range filtering. Only segments within the navigable channel, with relatively steady speed and weak external disturbances, are retained. To obtain a quasi-steady "deviation–thrust" statistical relationship, segments that enter a quasi-steady phase after thruster engagement are further extracted. The quasi-steady criterion is defined as $|\dot{\Delta\theta}(t)| < \varepsilon$ over a continuous window $T_s$. The window-averaged $\Delta\theta$ and $F_{test}$ are used to reduce random disturbance effects.

Under the assumption that the environmental compensation term $C_{env}$ is neglected, Equation (12) can be used to back-calculate the corresponding value for each quasi-steady sample.

$$k = \frac{F_{test,i}}{L^2 \cdot \sin(\Delta\theta_i)} \tag{14}$$

To improve noise robustness and reproducibility, a least-squares fit is applied to all samples to obtain a single global optimum $k$.

$$k^* = \underset{k}{\operatorname{argmin}} \sum_{i=1}^{N} \left( F_{test,i} - k\, L^2 \sin(\Delta\theta_i) \right)^2 = \frac{\sum_{i=1}^{N} F_{test,i} L^2 \sin(\Delta\theta_i)}{\sum_{i=1}^{N} \left( L^2 \sin(\Delta\theta_i) \right)^2} \tag{15}$$

The resulting $k^*$ is then used for online computation of the target thrust. In this study, the data source, thrust conversion method, data screening rules, quasi-steady criterion, and regression form are all explicitly defined, providing a complete specification of $k$ and its calculation procedure.

It should be noted that the AIS time resolution mainly affects high-frequency transients, whereas the calibration here targets a quasi-steady statistical relationship. In the subsequent simulation and control implementation, discretization is performed with $\Delta t$ = 0.2 s (5 Hz). This setting is used for closed-loop updates and short-horizon prediction, and it is used for a different purpose than the calibration stage.

In summary, this section establishes a decision chain of "heading-deviation identification–target push-thrust computation–control reference generation". The composite coefficient $k$ is obtained by calibrating full-scale bridge-area data. This provides a clear data basis and physical interpretability for the thrust mapping and improves the reproducibility of the proposed method.

## 4. Feedback Regulation and Adaptive Control of the Intelligent Push-Assisted System

Building on the target thrust $F_{push}$ derived in the previous section, this section designs an extended state observer (ESO) and a fuzzy self-tuning incremental PID controller, with a three-degree-of-freedom MMG model as the controlled plant. The controller generates the thruster-thrust command and incorporates feedforward compensation based on the lumped disturbance estimated by the ESO, enabling fast, smooth, and robust heading correction under yaw-deviation conditions in bridge areas.

### 4.1. Vessel Motion Model

In inland bridge reaches, heave, pitch, and roll have a limited influence on horizontal-plane motion, whereas planar motions (surge, sway, and yaw) dominate vessel trajectory tracking and heading control [33]. To simulate the vessel's dynamic response following intervention by the intelligent push-assisted device, this study incorporates hull hydrodynamics, propeller–rudder forces, and the external thruster-thrust input generated by the push-assisted device. A standard Maneuvering Modeling Group (MMG) approach is adopted to establish a three-degree-of-freedom (3-DOF) motion model for the target yaw-deviated vessel, as expressed in Equation (16) [34]:

$$\begin{cases} (m + m_y)\dot{v} = (m + m_y)\overline{u}_c \mathrm{r} + (m + m_x)\overline{u}_r r + Y_H + Y_p + Y_R + F_{push} \\ (m + m_x)\dot{u} - (m + m_x)\overline{u}_r r + (m + m_y)\overline{u}_c r = X_H + X_p + X_R \\ (I_{ZZ} + J_{ZZ})\dot{r} = N_H(v_r, u_r, r) + N_p(\overline{v}_r, \overline{u}_r, r) + N_R(\overline{v}_r, \overline{u}_r, r) + F_{push} \bullet L \end{cases} \tag{16}$$

In Equation (16), m is the vessel mass; $m_x$ and $m_y$ are the added masses in surge and sway, respectively. $u_r$ and $v_r$ denote the surge and sway velocities relative to the water at the center of gravity (CoG), while $\overline{u_r}$ and $\overline{v_r}$ represent the corresponding longitudinally averaged relative-water velocities along the vessel length. $r$ is the yaw rate. Similarly, $u_c$ and $v_c$ are the surge and sway current velocities at the CoG, with $\overline{u_c}$ and $\overline{v_c}$ denoting the corresponding longitudinally averaged current velocities along the vessel length. $\dot{u}$, $\dot{v}$ and $\dot{r}$ denote the surge and sway accelerations over ground and the yaw angular acceleration,

respectively. $I_{ZZ}$ and $J_{ZZ}$ are the yaw moment of inertia and the added yaw moment of inertia. The terms $(X_H, Y_H, N_H)$, $(X_P, Y_P, N_P)$, and $(X_R, Y_R, N_R)$ represent the surge force, sway force, and yaw moment acting on the hull, propeller, and rudder, respectively. The hull forces and moment are calculated using nonlinear models that account for nonlinear hydrodynamic derivatives, cross-flow drag effects, and nonlinear coupling among the rudder, propeller, and hull, thereby characterizing vessel maneuvering in bridge-area channels [35].

The proposed intelligent push-assisted device applies a single-point concentrated lateral push. Its point of application is located at the equivalent longitudinal position $x_p$ relative to the CoG (with the CoG as the origin and positive toward the bow). Since the device primarily provides lateral thrust and the longitudinal component is comparatively small, $X_{push} \approx 0$ is assumed. By modeling the push-assisted output as an equivalent lateral external force that generates a corresponding yaw moment, the thruster-thrust input term can be expressed as

$$X_{push} \approx 0,\ Y_{push} = Y_F F_{rad},\ N_{push} = N_F F_{rad} \tag{17}$$

Here, $F_{rad}$ denotes the final actuation thrust command issued to the push-assisted device (units: N). $Y_F$ and $N_F$ are the equivalent coefficients that map the thruster thrust to the sway force and yaw moment, respectively [36]. Assuming an ideal configuration in which the thrust direction aligns with the +y axis, $Y_F = 1$ and $N_F = x_p$; thus, $Y_{push} = F_{rad}$ and $N_{push} = F_{rad} \bullet x_p$. Furthermore, $F_{rad}$ is obtained by superimposing the controller output and the ESO-based compensation, as detailed in Sections 4.2 and 4.3. The hull sway hydrodynamic force and yaw moment consist of linear hydrodynamic-derivative terms and nonlinear cross-flow drag terms, as expressed in Equation (18):

$$\begin{cases} Y_H = \frac{1}{2}\rho d \int_{-\frac{L_{PP}}{2}}^{\frac{L_{PP}}{2}} C_D(x)(v_r(x) + xr)|v_r(x) + xr|dx \\ \qquad\qquad + \int_{-\frac{L_{PP}}{2}}^{\frac{L_{PP}}{2}} F_{push}(x)dx + Y_{\dot{v}}\dot{\overline{v}}_r + Y_{\dot{r}}\dot{r} \\ N_H = \frac{1}{2}\rho L_{PP} d \int_{-\frac{L_{PP}}{2}}^{\frac{L_{PP}}{2}} C_D(x)(v_r(x) + xr)|v_r(x) + xr|dx \\ \qquad\qquad + \int_{-\frac{L_{PP}}{2}}^{\frac{L_{PP}}{2}} F_{push}(x) \bullet x dx + N_{\dot{v}}\dot{\overline{v}}_r + N_{\dot{r}}\dot{r} \end{cases} \tag{18}$$

In Equation (18), ρ, d and $L_{pp}$ denote the water density, vessel draft, and length between perpendiculars, respectively. $C_D(x)$ represents the transverse drag coefficient at the longitudinal position $x$ along the hull. $Y_{\dot{v}}$, $N_{\dot{v}}$,$Y_{\dot{r}}$ and $N_{\dot{r}}$ are the linear hydrodynamic-derivative coefficients, with their specific values provided in [35]. This model integrates the linear maneuvering formulation with nonlinear cross-flow drag terms, thereby serving as the foundation for the ESO design in Section 4.2 and the control-law development in Section 4.3.

### *4.2. Extended State Observer (ESO) Design*

An extended state observer (ESO) lumps model uncertainty, unmodeled dynamics, and environmental disturbances into an extended state (i.e., a lumped disturbance), thereby reducing reliance on an accurate mathematical model and making it suitable for vessel

motion control under strong nonlinearity and complex disturbances [37]. For the 3-DOF dynamics incorporating thruster-thrust effects, these disturbances are modeled as an extended state as follows:

$$\begin{cases} f_u = \frac{X_w + \Delta F_u}{m + m_x} \\ f_v = \frac{Y_W + \Delta F_v}{m + m_y} \\ f_r = \frac{N_r + \Delta F_r}{I_{ZZ} + J_{ZZ}} \end{cases} \tag{19}$$

where $\Delta F_u$, $\Delta F_v$ and $\Delta F_r$ denote the unmodeled dynamics and external disturbances in surge, sway, and yaw, respectively (encompassing wind–current loads and parameter perturbations). The extended state vector is defined as $Z = [\mathrm{uvr} f_u f_v f_r]^T$, which augments the vessel motion states with the lumped disturbance terms. By employing linear state error feedback, the ESO estimates the true system states in real time. The ESO dynamics are given as follows:

$$\begin{cases} \dot{\hat{u}} = \frac{X_H + X_{PR}}{m + m_x} + \frac{(m + m_y)\overline{v}_r \hat{r}}{m + m_x} + \hat{r}\overline{v}_C + \hat{f}_u + L_1(u - \hat{u}) \\ \dot{\hat{v}} = \frac{Y_H + Y_{PR}}{m + m_y} + \frac{(m + m_x)\overline{u}_r \hat{r}}{m + m_y} - \hat{r}\overline{u}_C + \hat{f}_v + L_2(v - \hat{v}) \\ \dot{\hat{r}} = \frac{N_H + N_{PR}}{I_{ZZ} + J_{ZZ}} + \hat{f}_r + L_3(v - \hat{v}) \\ \dot{\hat{f}}_u = L_4(u - \hat{u}) \\ \dot{\hat{f}}_v = L_5(v - \hat{v}) \\ \dot{\hat{f}}_r = L_6(r - \hat{r}) \end{cases} \tag{20}$$

where $\hat{u}$, $\hat{v}$, and $\hat{r}$ denote the estimated vessel states; $\hat{f}_u$, $\hat{f}_v$, and $\hat{f}_r$ represent the estimated disturbance terms; and $L_1, L_2, L_3, L_4, L_5, L_6$ are the observer gains. The performance of the ESO relies on appropriate tuning of the gain matrix $L$. Using a bandwidth-parameterization approach, the gains are expressed in terms of the observer bandwidth $\omega_0$ as follows:

$$L = \begin{bmatrix} 3\omega_0 & 0 & 0 & 3\omega_0^2 & 0 & 0 \\ 0 & 3\omega_0 & 0 & 0 & 3\omega_0^2 & 0 \\ 0 & 0 & 3\omega_0 & 0 & 0 & 3\omega_0^2 \end{bmatrix}^T \tag{21}$$

The observer bandwidth $\omega_0$ is selected to satisfy the system's sampling constraints and dynamic-response requirements:

$$\omega_0 \geq 2 \times \max\left\{ \left|\frac{\partial i}{\partial u}\right|, \left|\frac{\partial i}{\partial v}\right|, \left|\frac{\partial i}{\partial r}\right| \right\} \tag{22}$$

The disturbance terms estimated by the ESO are incorporated into the control system via feedforward compensation. The compensation coefficient matrix is derived from the vessel inertia parameters and rudder effectiveness coefficients:

$$\gamma = \begin{bmatrix} \frac{m + m_x}{X_\delta} & 0 & 0 \\ 0 & \frac{m + m_y}{Y_\delta} & 0 \\ 0 & 0 & \frac{I_{zz} + J_{zz}}{N_\delta} \end{bmatrix} \tag{23}$$

where $X_\delta, Y_\delta$, and $N_\delta$ denote the thruster-thrust coefficients relating the thrust input to the surge force, sway force, and yaw moment, respectively; their computation is detailed in [38].

### 4.3. Fuzzy Self-Tuning PID Control and Disturbance Rejection

Fuzzy logic inference can accommodate nonlinearity, time-varying behavior, and uncertainty by adjusting PID parameters online based on the error and its rate of change, thereby improving adaptability and control accuracy under complex operating conditions.

In an incremental PID controller, the output is the increment of the control input, which mitigates fluctuations in the control signal. This characteristic is well suited to ship steering dynamics, which typically exhibit slow response and hysteresis. Accordingly, a fuzzy self-tuning incremental PID controller is developed by integrating fuzzy logic with an incremental PID strategy [39]. It achieves robust thruster-thrust regulation through five components: definition of input variables, fuzzification, rule-base construction, defuzzification, and control-law formulation.

4.3.1. Fuzzy Incremental PID Controller Design

(1) Input variable definition. The controller inputs are defined as the thruster-thrust error (e) and the error change rate $\Delta e$:

$$e(k) = F_{push}(k) - F_{rad}(k) \tag{24}$$

$$\Delta e(k) = e(k) - e(k-1) \tag{25}$$

where $F_{push}$ denotes the target thruster thrust, and $F_{rad}$ represents the actual thruster thrust acting on the vessel.

(2) Fuzzification and membership functions.

A seven-level fuzzy linguistic set is employed to describe the input–output behavior, defined by the fuzzy subsets {NB, NM, NS, ZE, PS, PM, and PB}. Symmetric triangular membership functions are adopted:

$$\mu_A(x) = \max\left\{0, 1 - \frac{|x - c_i|}{w_i}\right\} \tag{26}$$

where $\mu$ denotes the membership degree; c is the center of the i-th fuzzy set; and $\omega$ represents the width of the support domain. The output variable $K_P$ is partitioned using exponential scaling, defined by the fuzzy subsets {VL, L, ML, M, MH, H, and VH}. The variables $T_i$ and $T_d$ are partitioned on a logarithmic scale, with fuzzy subsets {VS, S, MS, M, ML, L, and VL}.

(3) Fuzzy rule-base construction.

Based on vessel maneuvering characteristics and expert knowledge, 49 fuzzy rules are established. Representative examples are listed below.

Rule 1: If $e = NB$ and $\Delta e = NB$ then $K_P$ = VH, $T_i$ = VS, and $T_d$ = VL. This corresponds to emergency correction when the vessel initially deviates significantly from the target heading.

Rule 2: If $e = NM$ and $\Delta e = PM$ then $K_P = MH$, $T_i$ = MS, and $T_d$ = S. This represents a transitional state with a moderate error but a trend toward convergence.

Rule 3: If $e = PS$ and $\Delta e = NS$ then $K_P = M$, $T_i$=$M$, and $T_d = M$. This applies to fine-tuning control with a small error and a reverse-correction tendency.

(4) Defuzzification.

Once fuzzy inference generates the output fuzzy sets, the centroid method is employed to defuzzify the results into crisp values, calculated as follows:

$$\sigma = \frac{\sum_{j=1}^{n} x_j \mu_j}{\sum_{j=1}^{n} \mu_j} \tag{27}$$

where $\sigma$ is the defuzzified crisp output, and $x_i$ and $u_j$ denote the j-th discrete universe value and its membership degree, respectively.

(5) Incremental PID control law.

Consider the sampling period $T_s$ of the discrete-time system. The first-order difference in the error is defined as $\Delta e(k) = e(k) - e(k-1)$, and the second-order difference is defined as $\Delta^2 e(k) = e(k) - 2e(k-1) + e(k-2)$. The increment of the push thrust, $\Delta F(k)$, is computed as follows:

$$\Delta F(k) = K_p \Delta e(k) + K_P \frac{T_s}{T_i} e(k) + K_P \frac{T_d}{T_s} \Delta^2 e(k) \tag{28}$$

The output of the fuzzy self-tuning incremental PID controller is given by

$$F_{pid}(k) = F_{pid}(t-1) + \Delta F(k) \tag{29}$$

To ensure actuator safety and smooth control action, the practical output is recommended to be subject to magnitude limits and rate constraints:

$$F_{pid}(k) \leftarrow sat\left(F_{pid}(k), -F_{\max}, F_{\max}\right) \tag{30}$$

4.3.2. Disturbance-Rejection Strategy

The disturbance-rejection strategy achieves active compensation by integrating the ESO-estimated equivalent disturbance with the output of the fuzzy self-tuning incremental PID controller [40]. Considering the limited capability of the push-assisted device to compensate for longitudinal disturbances, the strategy focuses primarily on mitigating disturbances in the sway and yaw channels. The ESO-estimated equivalent disturbance vector is defined as $\hat{F} = \begin{bmatrix} \hat{f}_u & \hat{f}_v & \hat{f}_r \end{bmatrix}$. This vector is mapped to a compensation thrust via $f_{cmp} = \gamma_{22}\hat{f}_v + \gamma_{33}\hat{f}_r$. The final compensated output is then formulated as

$$F_{rad}(k) = F_{pid}(k) + f_{cmp}(k) \tag{31}$$

where $F_{pid}$ denotes the command generated by the fuzzy self-tuning incremental PID controller, and $f_{cmp}$ represents the compensation term.

Accordingly, this study establishes a comprehensive closed-loop control framework that integrates KF-based state estimation and short-horizon prediction, yaw-deviation identification, and target-thrust reference determination. By combining the MMG vessel motion model with ESO-based disturbance compensation and fuzzy self-tuning incremental PID control, the thrust command $F_{pid}$ is superimposed with $f_{cmp}$ to yield the final actuation thrust $F_{rad}$ for heading correction [41]. This architecture provides a methodological basis for implementable active intervention following bridge-area early warnings.

## 5. Experiments and Results

### *5.1. Simulation Setup*

5.1.1. Objectives and Approach

This study conducts numerical simulations for a typical high-risk inland bridge scenario described as "sudden yaw—pier approach—corrective recovery." The objectives are defined at three levels.

1. Effectiveness.

Under identical vessel parameters, initial speed, and yaw trigger conditions, "rudder-only recovery" is compared with "pushing-assisted intervention." The comparison focuses on heading convergence rate, lateral deviation, and minimum pier clearance. The aim is to quantify the improvement in recovery efficiency and safety margin brought by the additional lateral thrust degree of freedom.

2. Algorithmic contribution.

With the thruster enabled, a conventional PID thruster controller is used as a benchmark. This separates two factors: the effect of adding a lateral thrust actuator, and the effect of the intelligent control design, including Kalman-based state estimation and prediction, and ESO-based disturbance compensation. Their respective contributions to corrective performance are evaluated.

3. Robustness and generalization.

To avoid conclusions based on a single calm-water case, a parameter sensitivity analysis is conducted. The effects of initial yaw angle, vessel speed, and thruster activation delay on key metrics are examined. At least one case with explicit external disturbance, such as cross-current or lateral external moment, is included. This tests the ESO disturbance rejection capability and overall robustness under environmental disturbance and modeling error.

A controlled comparative design is adopted. All conditions except the control strategy remain unchanged. Three groups are defined: rudder-only (no thruster), conventional thruster (PID control), and intelligent thruster (state estimation and prediction trigger with ESO compensation). Heading recovery, lateral deviation, and pier clearance are compared to quantify both the effect of enabling lateral thrust and the impact of different control strategies.

#### 5.1.2. Simulation Scenarios and Evaluation Metrics

1. Experimental scenario and coordinate system

A straight inland bridge reach is selected as the test scenario. A one-way navigation channel is defined, and the channel centerline is taken as the planned route. A global coordinate system O−xy is established. The $x$ is aligned with the channel centerline and points downstream. The $y$-axis is lateral. The vessel position is described by the center-of-mass coordinates $(x(t), y(t))$, as shown in Figure 3. The heading angle $\theta(t)$ is defined with respect to the channel centerline. $\theta = 0$ indicates straight sailing along the channel.

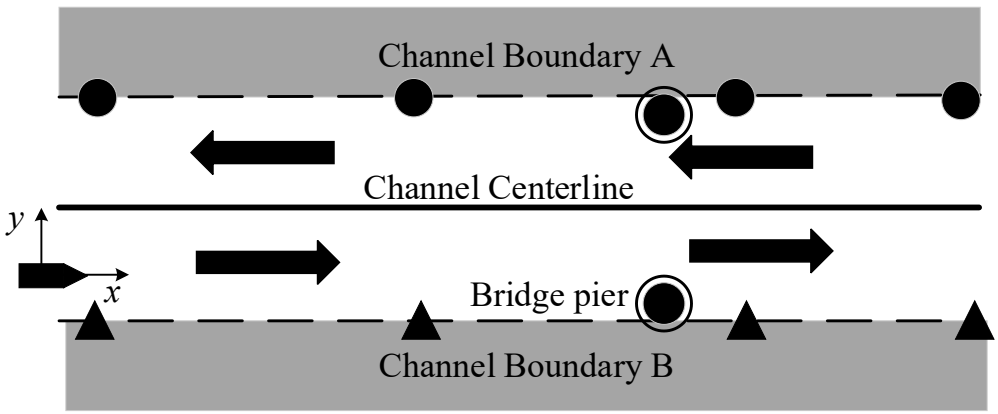



**Figure 3.** Schematic of the bridge-area navigation channel.

A bridge span is arranged at the middle of the reach. Two piers are placed on both sides of the channel. Their geometric boundaries are modeled as equivalent cylinders. This representation is used to compute the minimum clearance and collision-avoidance margin during yaw motion.

The controlled vessel is the inland cargo ship XINYI 5658. Its principal particulars are listed in Table 1.

**Table 1.** Parameters of the downstream cargo vessel.

| Parameter | Value |
|---|---|
| Vessel name | XINYI5658 |
| Length (m) | 108 |
| Beam (m) | 18 |
| Draft (m) | 6 |
| Speed (kn) | 5 |

2. Simulation conditions and control group design

At the initial time, the vessel sails steadily along the channel centerline. The initial speed is set to $V = 5$ kn, and the rudder angle is zero. To simulate sudden yaw in the bridge area, an initial heading deviation $\Delta\theta_0 = 10^\circ$ is imposed at $t = t_{yaw}$, while sufficient longitudinal clearance from the pier remains. This generates the full process as follows: steady sailing—yaw onset—yaw development—control intervention—heading recovery.

The total simulation time is $T = 260$ s, and the sampling interval is $\Delta t = 0.2$ s. The baseline case is conducted in calm water. Wind, wave, and current disturbances are neglected.

A controlled comparative design is adopted.

Group A is the rudder-only recovery group (no thruster).

Group B is the conventional PID thruster group. The thrust command is generated from lateral deviation and its rate, without state fusion or disturbance compensation.

Group C is the intelligent thruster group. It integrates state estimation, risk-trigger logic, and ESO-based disturbance compensation, and cooperates with rudder control for correction.

All other parameters and initial conditions are identical across groups. Differences in results are therefore attributed to the control strategy.

3. Thruster intervention mechanism

In Group C, fused estimation provides vessel position, speed, and heading. The deviation between predicted heading and reference heading is defined as $\Delta\theta(t)$. The threshold is set to $\Delta\theta_{th} = 5^\circ$. A consecutive decision rule is applied. If $|\Delta\theta(t)|$ exceeds the threshold for three successive sampling steps, yaw risk is identified and thruster intervention is activated.

This trigger allows early action during yaw development. It reduces correction delay caused by vessel inertia under rudder-only control.

For stability analysis, a thruster activation delay $\boldsymbol{\tau_a}$ is introduced in the sensitivity study. After the trigger condition is satisfied, the thrust command is applied with a delay of $\boldsymbol{\tau_a}$ seconds. This models the delay in the sensing–decision–actuation chain.

4. Stability verification: sensitivity analysis design

A single calm-water case is insufficient to assess stability. A sensitivity analysis is therefore conducted. The objective is to evaluate performance retention under varying conditions.

Three key parameters are considered: initial yaw angle $\Delta\theta_0$, vessel speed $V$, and thruster activation delay $\boldsymbol{\tau_a}$. The parameter $\Delta\theta_0$ represents the magnitude of sudden yaw. The speed $V$ affects maneuverability and the available correction window. The delay $\boldsymbol{\tau_a}$ reflects implementation latency in practical systems. The parameter sets are defined as $\Delta\theta_0 \in \{5^\circ, 10^\circ, 15^\circ\}$, $V \in \{4,5,6\}$ kn, $\tau_a \in \{0,5,10\}$s.

Discrete combinations are tested. For each combination, the three control strategies are executed. Key metrics, including lateral deviation error $\mathbf{Y_{er}}$ and minimum pier clearance $\mathbf{D_{min}}$, are statistically analyzed. The results support quantitative conclusions on robustness and transferability.

## 5. ESO performance verification: external disturbance scenario

To evaluate the ESO under external disturbance beyond modeling error, a cross-current case is introduced in addition to the calm-water baseline. For $t \geq t_{yaw}$, a constant lateral current $V_c = 0.5\,m/s$ is applied until the end of simulation.

Under this condition, the conventional PID thruster group and the intelligent thruster group are compared in terms of heading convergence, lateral deviation control, and minimum pier clearance. The disturbance compensation mechanism is interpreted through ESO estimates and thrust response. This verifies the effectiveness and robustness of the proposed method under dual uncertainties: environmental disturbance and modeling error.

To quantify the differences between yaw development and active intervention phases, the evaluation metrics listed in Table 2 are adopted.

**Table 2.** Evaluation metrics used in the simulation study.

| Evaluation Metrics | Symbol | Description |
|---|---|---|
| Heading deviation | $\Delta\theta(t)$ | Reflects the growth of heading error after yaw onset and its decay after thruster intervention. |
| Recovery time | $T_{re}$ | Measures recovery efficiency. |
| Maximum lateral deviation | $Y_{er}$ | Evaluates yaw development severity and trajectory re-alignment capability. |
| Minimum pier clearance | $D_{min}$ | Indicates the minimum collision-avoidance safety margin. |

### *5.2. Results and Analysis*

Based on the sudden yaw scenario and control group design defined in Section 5.1, the vessel responses under three control strategies are compared:

A—rudder-only correction;

B—conventional PID thruster assistance;

C—intelligent thruster-assisted correction integrating state estimation, risk-trigger logic, and ESO-based disturbance compensation.

After yaw onset, all cases show lateral deviation toward the pier side, as illustrated in Figure 4.

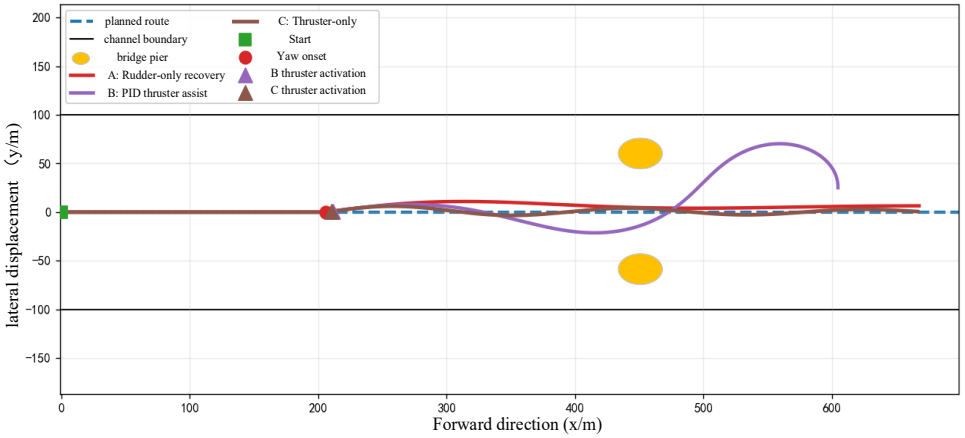



**Figure 4.** Comparative trajectories under different bridge-area operating conditions.

In Group A (rudder-only), lateral deviation continues to increase during yaw development. Due to vessel inertia and rudder response lag, heading recovery is slow. As a result, significant lateral error remains at critical longitudinal positions in the bridge area, leading to reduced pier clearance and a smaller safety margin.

In Group B (PID thruster), lateral thrust limits further deviation once activated and drives the trajectory back toward the centerline. However, noticeable overshoot and oscillation occur during recovery. This behavior reflects the susceptibility of lateral-error-based PID thrust control to dynamic coupling and phase lag.

In Group C (intelligent thruster), intervention occurs earlier once the risk trigger condition is satisfied. Disturbance compensation and damping effects yield smoother correction. The peak lateral deviation is smaller, recovery is faster, and trajectory tracking is more stable. Lateral error is reduced before the vessel reaches sensitive bridge positions, thereby enhancing overall navigation safety margin.

The trajectory differences are further supported by the heading deviation responses in Figure 5. After yaw onset, $\Delta\theta(t)$ in all three groups follows an "error growth–control intervention–error decay" process, but their convergence behaviors differ. In Group A, the deviation decays most slowly and a noticeable residual persists, indicating the limited corrective capability of rudder-only control under high inertia. In Group B, the deviation decreases faster after thruster activation, but oscillation and overshoot near the zero-crossing are more pronounced, showing a faster yet less stable response. In Group C, once the trigger condition is satisfied and intervention becomes effective, both the peak deviation and oscillation amplitude are suppressed, and the response converges in a more monotonic and better-damped manner. This suggests that the intelligent thruster not only reduces lateral track offset but also improves the decay characteristics of yaw dynamics, thereby enhancing heading recovery efficiency and stability. The red line in the figure represents the moment of thruster activation, while the yellow line indicates the yaw onset, helping to clearly display the intervention moments and their corresponding responses in each group.

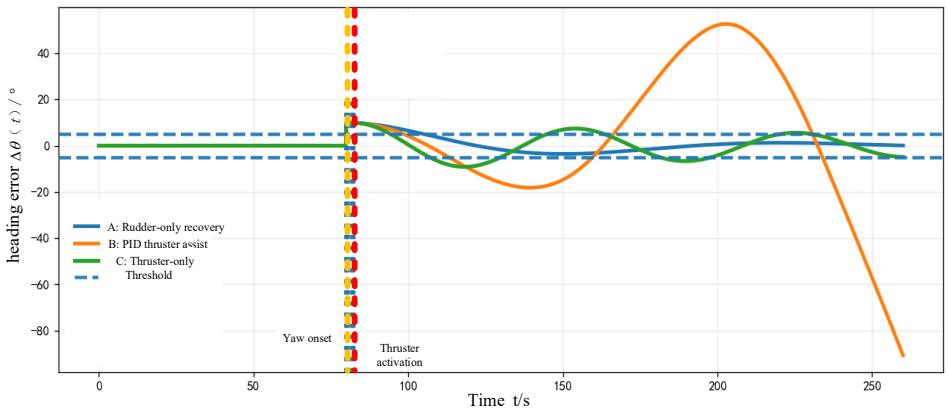



**Figure 5.** Comparative heading deviation responses under different operating conditions.

The thruster output profiles further explain the differences in trajectory and heading responses between Groups B and C, as shown in Figure 6. In Group B, the thrust exhibits larger temporal fluctuations, frequent sign reversals, and higher amplitude segments. This indicates that the control law is mainly driven by lateral deviation and its rate and is therefore prone to a "correction–overshoot–re-correction" cycle under phase lag and dynamic coupling.

In contrast, Group C shows earlier intervention, smoother variation, and better-controlled peak thrust. This reflects the anticipatory nature of risk-triggered activation and the effect of ESO-based disturbance compensation in reducing phase lag and high-frequency excitation. As a result, heading and trajectory corrections are achieved more effectively with lower-control energy fluctuation.

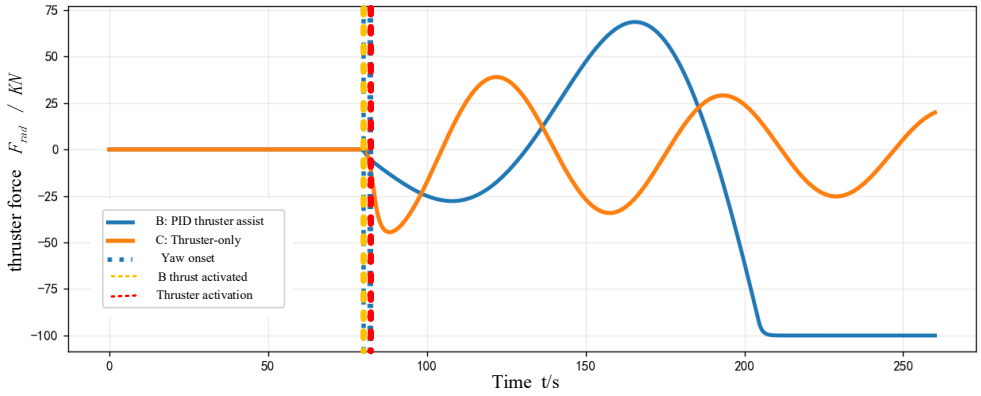
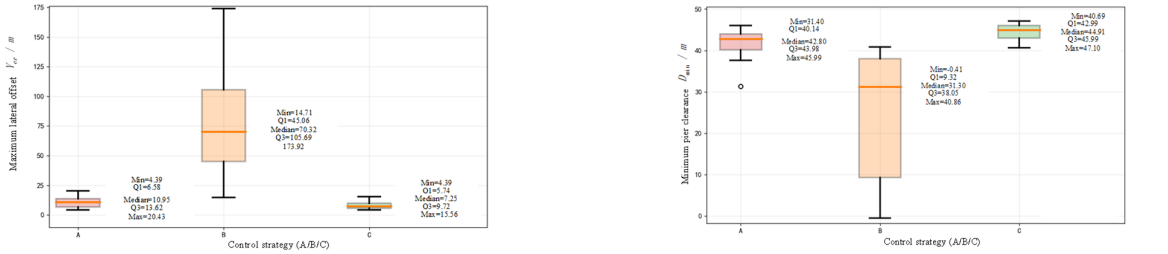



**Figure 6.** Heading response and thrust activation under different control strategies.

To obtain quantitative conclusions, the key performance indices under the sensitivity parameter combinations are statistically compared, as shown in Figure 7. For the maximum lateral deviation $Y_{er}$, Group C exhibits a lower median and a narrower interquartile range. This indicates more effective suppression of peak lateral deviation during yaw development and a more stable recovery process. Group B shows moderate improvement, but with a wider distribution, reflecting greater sensitivity to oscillation and overshoot under varying conditions. Group A performs worst, with larger overall deviation and more pronounced dispersion.




(**a**) Box plot of maximum lateral deviation $Y_{er}$ (**b**) Box plot of minimum distance to pier $D_{min}$

**Figure 7.** Box plots of maximum lateral deviation $Y_{er}$ and minimum distance to pier $D_{min}$.

For the minimum pier clearance $D_{min}$, Group C maintains a higher overall distribution, indicating a larger collision-avoidance safety margin at the most critical instant. Group B ranks intermediate, whereas Group A more frequently approaches the risk boundary.

To further examine the influence of key operating parameters on performance retention, the main effects of initial yaw angle $\Delta\theta_0$, vessel speed $V$, and thruster activation delay $\boldsymbol{\tau_a}$ on $Y_{er}$ and $D_{min}$ are analyzed. The corresponding trends are presented in Figures 8 and 9.

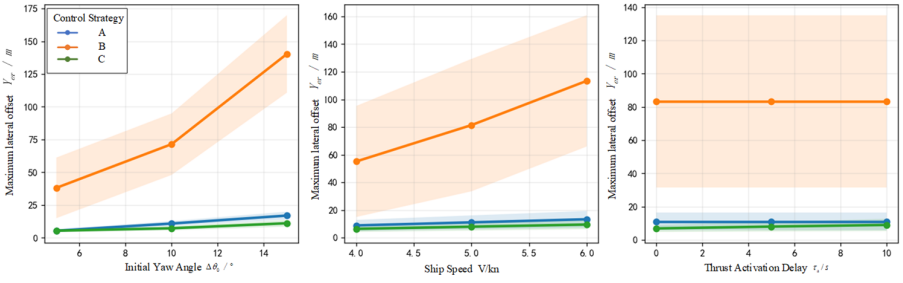



**Figure 8.** Maximum lateral deviation Y_er under different control strategies.

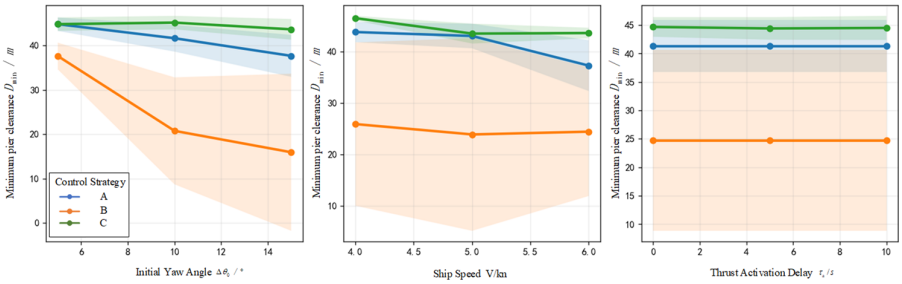



**Figure 9.** Minimum distance to pier $D_{min}$ under different control strategies.

In the figures, the main-effect curve represents the mean value $\mu$ obtained by averaging over all discrete combinations of the remaining parameters at each fixed level of a single parameter. The shaded band denotes the standard deviation range $\mu \pm 1\sigma$, which characterizes the dispersion of the metric under different parameter combinations. The corresponding $\mu$, $\sigma$, and sample size n are summarized in Table 3 for $Y_{er}$ and Table 4 for $D_{min}$, allowing verification of the bandwidth magnitude and sources of variability.

**Table 3.** Main-effect statistics of maximum lateral deviation $Y_{er}$ (μ ± σ, unit: m).

| Factor | Value | Group A | Group B | Group C |
|---|---|---|---|---|
| $\Delta\theta_0$(°) | 5 | 5.486 ± 0.950 | 38.163 ± 23.102 | 5.486 ± 0.950 |
| | 10 | 10.947 ± 1.896 | 71.517 ± 23.451 | 7.350 ± 1.631 |
| | 15 | 17.026 ± 2.949 | 140.340 ± 29.556 | 11.188 ± 2.503 |
| V(kn) | 4 | 8.923 ± 4.000 | 55.153 ± 40.117 | 6.452 ± 2.242 |
| | 5 | 11.153 ± 4.999 | 81.440 ± 47.849 | 8.014 ± 2.766 |
| | 6 | 13.384 ± 5.999 | 113.427 ± 47.439 | 9.558 ± 3.278 |
| $\tau_a$(s) | 0 | 11.153 ± 5.421 | 83.340 ± 51.851 | 6.937 ± 2.110 |
| | 5 | 11.153 ± 5.421 | 83.340 ± 51.851 | 8.059 ± 2.917 |
| | 15 | 11.153 ± 5.421 | 83.340 ± 51.851 | 9.028 [1] ± 3.664 [2] |

[1] μ denotes the mean value obtained by averaging over all discrete combinations of the other two factors at a fixed level of the considered factor; [2] σ denotes the standard deviation; the sample size is n = 9.

**Table 4.** Main-effect statistics of minimum pier clearance $\mathbf{D}_{min}$ (μ ± σ, unit: m).

| Factor | Value | Group A | Group B | Group C |
|---|---|---|---|---|
| $\Delta\theta_0$(°) | 5 | 44.810 ± 1.515 | 37.620 ± 3.009 | 44.810 ± 1.515 |
| | 10 | 41.642 ± 3.020 | 20.752 ± 12.060 | 45.162 ± 1.517 |
| | 15 | 37.662 ± 4.729 | 15.925 ± 17.714 | 43.641 ± 2.328 |
| V(kn) | 4 | 43.802 ± 1.973 | 25.928 ± 15.863 | 46.499 ± 0.442 |
| | 5 | 43.034 ± 2.391 | 23.915 ± 18.711 | 43.502 ± 1.929 |
| | 6 | 37.278 ± 4.943 | 24.454 ± 12.490 | 43.612 ± 1.016 |
| $\tau_a$(s) | 0 | 41.371 ± 4.570 | 24.766 ± 15.918 | 44.683 ± 1.732 |
| | 5 | 41.371 ± 4.570 | 24.766 ± 15.918 | 44.420 ± 1.985 |
| | 15 | 41.371 ± 4.570 | 24.766 ± 15.918 | 44.510 ± 2.114 |

In general, increasing $\Delta\theta_0$ amplifies lateral deviation accumulation during yaw development and reduces the available correction window in the bridge area. As a result, $Y_{er}$ increases and $D_{min}$ decreases for all three strategies. Variations in vessel speed and activation delay also lead to performance degradation to different extents. In particular, increasing $\boldsymbol{\tau_a}$ postpones thruster intervention and is a key factor contributing to further reduction of $D_{min}$.

Comparing the mean levels and dispersion bands across parameter levels shows that Group C consistently maintains lower $Y_{er}$ and higher $D_{min}$, with narrower standard deviation bands and lower sensitivity to parameter variation. Group B improves the mean

performance but exhibits larger fluctuations under certain combinations. Group A degrades most significantly under adverse parameter settings. These results demonstrate that the proposed intelligent thruster-assisted strategy preserves stability and robustness under variations in yaw intensity, vessel speed, and execution delay.

To further validate the proposed method under dual uncertainties arising from external disturbance and modeling error, Figures 10–14 present the system responses and observer estimation results for a typical bridge scenario with a constant cross-current $V_c = 0.5\,\mathrm{m/s}$.

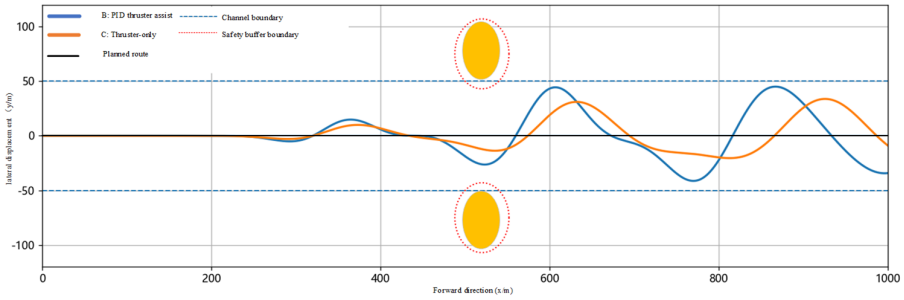



**Figure 10.** Vessel trajectories under different thruster strategies with cross-current disturbance.

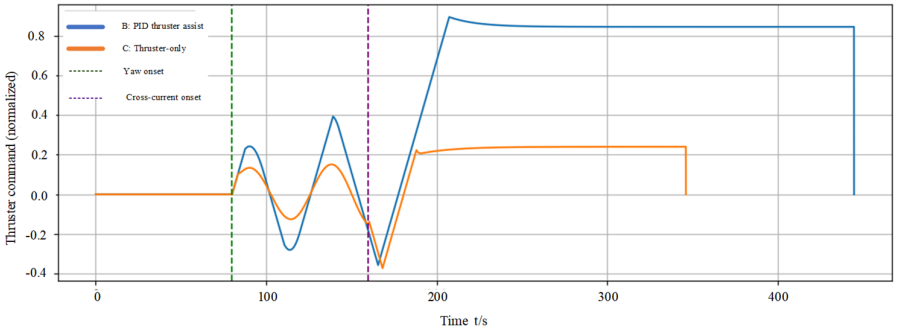



**Figure 11.** Comparison of thruster responses under different thruster control strategies.

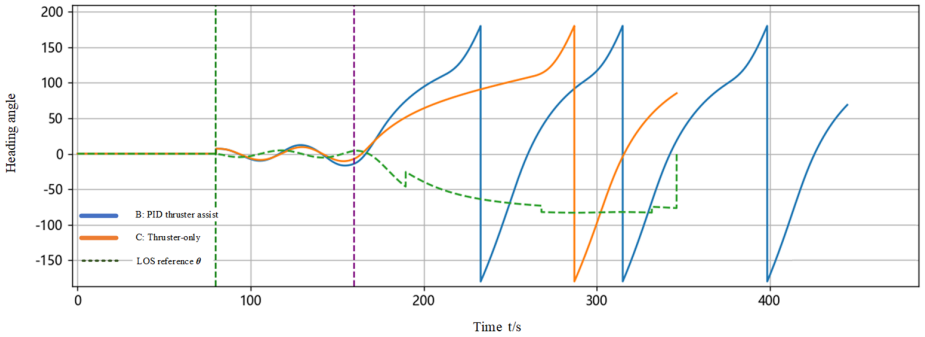



**Figure 12.** Comparison of heading angle responses.

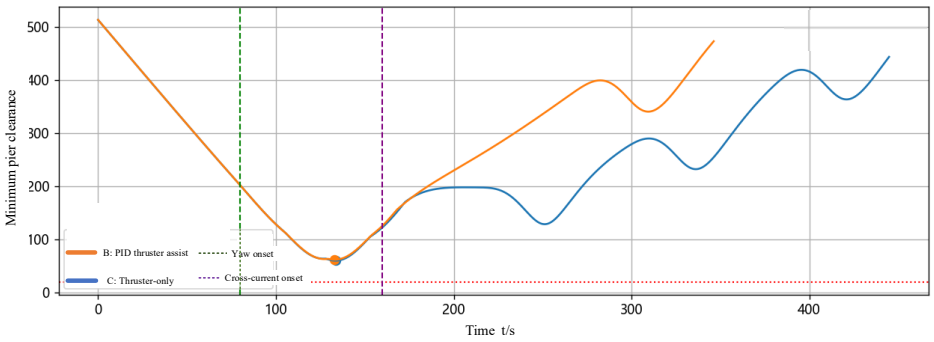
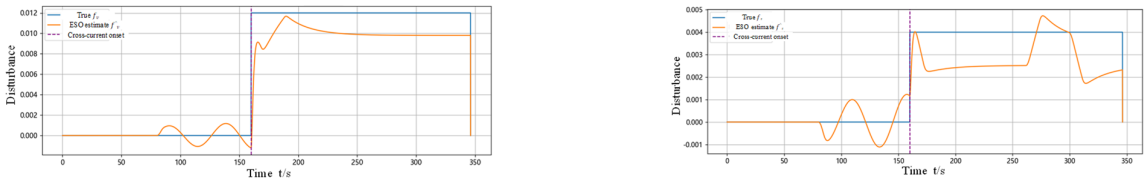



**Figure 13.** Minimum distance to the bridge pier under different control strategies.




(**a**) (**b**)

**Figure 14.** ESO disturbance estimation results under cross-current conditions. (**a**) Comparison of disturbance estimation in the sway channel $f_v$. (**b**) Comparison of disturbance estimation in the yaw channel $f_r$.

Figure 10 compares the vessel trajectories of Groups B and C under cross-current conditions. In both groups, yaw disturbance leads to deviation from the planned route. After the cross-current is applied at t $\geq t_{yaw}$, lateral drift accumulates more rapidly. In comparison, Group C initiates effective corrective intervention at an earlier stage, resulting in smaller deviation amplitude and reduced oscillation during recovery. It also maintains a larger collision-avoidance margin in the vicinity of the bridge pier. The blue solid line represents the PID thruster assist trajectory, which uses a combination of PID control and thruster assistance for correction, while the orange line represents the thruster-only control trajectory, which relies solely on the thruster for correction. The black dashed line shows the planned route, serving as a reference for comparison.

Figure 11 presents the comparison of thruster responses. In Group B, thrust fluctuations and oscillatory variations are more evident after activation. In contrast, Group C exhibits smoother output, and the intervention intensity is adaptively scheduled according to risk level and estimated disturbance. This enables a balance between corrective efficiency and actuation smoothness.

Figure 12 illustrates the heading response ($\boldsymbol{\theta}$ = 0 aligned with the channel centerline). After the cross-current is introduced, a steady-state heading offset is required to counteract lateral drift. The purple line represents the cross-current onset. Group C achieves faster convergence with smaller oscillation, indicating improved dynamic damping and heading regulation performance.

Figure 13 compares the minimum pier clearance $\mathbf{D}_{min}$. Group C maintains a higher overall level, and its minimum value remains farther from the risk boundary. This indicates that effective trajectory recovery is achieved while preserving a larger lower bound of safety margin. The red dashed line represents the collision threshold distance to the bridge pier.

Figure 14a,b present the ESO disturbance estimation results. As the simulation focuses on bridge-area correction with lateral thrust, the vessel dynamics are modeled primarily in the sway (v) and yaw (r) channels. Therefore, only the extended disturbances $f_v$ and $f_r$ are estimated and analyzed.

The results show that, after activation of the cross-current, the ESO rapidly tracks disturbance variations. The estimates $\hat{f}_v$ and $\hat{f}_r$ are fed forward into the control law, supporting transient suppression of error accumulation and improved steady-state disturbance rejection.

Figures 10–14 demonstrate, from both response characteristics and mechanism analysis, that under combined cross-current disturbance and modeling error, the proposed intelligent thruster-assisted strategy achieves more stable trajectory recovery and maintains a more reliable safety margin in the bridge area. This further confirms its stability and robustness.

In summary, Figures 4–9 consistently show, from both typical response analysis and statistical trends, that thruster intervention significantly alters yaw development and recovery after disturbance onset. In Group A, correction relies solely on rudder action, leading to pronounced lateral deviation accumulation and delayed recovery. In Group B,

PID-based thruster assistance improves recovery speed and reduces deviation; however, thrust fluctuation and response oscillation are more evident during intervention, and performance is more sensitive to adverse parameter combinations. In contrast, Group C integrates risk-trigger logic, state fusion, and disturbance compensation to achieve earlier and smoother thrust engagement. As a result, it attains lower maximum lateral deviation $Y_{er}$ and larger minimum pier clearance $D_{min}$. Its main-effect means degrade more gradually and exhibit narrower dispersion bands, indicating improved stability and robustness.

Figures 10–14 extend these findings to scenarios with dual uncertainties, namely cross-current disturbance combined with modeling error. After introducing a constant cross-current, both Groups B and C experience increased lateral drift and greater heading regulation demand. Nevertheless, Group C maintains more stable trajectory recovery, smaller heading oscillation, and a higher lower bound of bridge-area safety margin. Its thrust response remains smoother and more targeted. The ESO estimation results in Figure 14 show that, in the sway (v) and yaw (r) channels considered in this study, the disturbance terms $f_v$ and $f_r$ are effectively tracked and utilized for feedforward compensation. This mechanism supports cross-current rejection and suppresses error accumulation. Overall, under nominal conditions, parameter variations, and external cross-current disturbance, Group C consistently balances trajectory controllability and bridge-area safety margin, meeting the integrated requirements of stability, robustness, and safety redundancy in bridge navigation.

## 6. Discussion

### *6.1. Mechanistic Interpretation and Method Positioning*

Yaw-deviation correction in bridge areas is a problem of disturbance suppression and rapid trajectory reconstruction in a constrained space. The objective is to suppress the growth of lateral error and restore the safety margin within a limited response window, rather than conventional heading keeping. Rudder-only control mainly relies on yaw–sway coupling to generate corrective motion. Due to vessel inertia and hydrodynamic lag, lateral deviation often continues to accumulate during the yaw-development phase.

With push assistance, the system changes from a single-input structure (rudder) to a dual-input structure with a direct lateral-force channel. This allows lateral momentum to be modulated directly at an early stage of yaw deviation. From a control perspective, the effective control authority in the lateral channel is enhanced. This changes the slope of error evolution and improves the controllability of the recovery process. This interpretation is consistent with classical maneuvering theory on coupled sway–yaw dynamics [41].

This study does not introduce a new fundamental control principle. The Kalman filter, ESO, and fuzzy self-tuning PID are established tools. The focus is on bridge-area risk scenarios. The chain of "state estimation and short-horizon prediction–yaw-deviation identification–push-assist decision–closed-loop control" is organized to be directly executable. This shifts the control objective from conventional attitude/trajectory regulation to a safety-margin-oriented risk-handling task. It extends risk response from the information layer to the execution layer.

### *6.2. Robustness and Applicability Boundaries Under External Disturbances*

When external disturbances, such as cross-currents, act continuously, the system typically needs to reach a new equilibrium to counter the drift tendency. Under rudder-only control, hydrodynamic lag and yaw inertia can compress the safety margin in critical segments. The ESO lumps model uncertainty, unmodeled dynamics, and environmental disturbances into an extended state and estimates it online. As a result, the disturbance terms (the $f_v$ and $f_r$ terms associated with the $v$ and $r$ channels in this study) can be

approximated and injected into the control law in a feedforward form. This reduces error accumulation at the early stage of disturbance action and provides the necessary balancing effort at steady state. This mechanism is consistent with the ADRC/ESO principle of "total disturbance estimation and compensation" [42]. In this study, it is further coupled with risk triggering and push-assist scheduling, so that the anti-disturbance capability can be reflected by safety indicators such as the minimum clearance to bridge piers.

This study is validated using a simplified three-DOF model and a limited set of operating conditions. When shallow-water nonlinear hydrodynamics, strong transient crosswind disturbances, and actuator response lag are considered, the control performance may degrade to varying degrees. Under thrust saturation, rate limits, or large execution delays, the achievable improvement in safety margin will also be constrained. Therefore, the proposed method is best viewed as an engineering framework with basic robustness, and it requires parameter matching and tuning for specific bridge-area environments and vessel types. Future work should conduct sensitivity analyses under a wider range of wind–wave–current and shallow-water conditions and incorporate thrust and energy-consumption constraints into a unified design and evaluation.

### *6.3. Engineering Implementability and Implications for Bridge-Area Safety Governance*

The "execution layer" in this study does not refer to deploying a complex system onboard the vessel. It refers to a shore-based push-assist device deployed in bridge areas. The device is fixed at critical channel segments and can operate unattended. It obtains approaching-vessel states through shore-based AIS, radar, and vision sensing. An embedded control unit performs estimation, identification, and command computation, and then drives the push-actuation mechanism to execute the intervention. In terms of computational complexity, the Kalman filter, ESO, and incremental PID involve low-order real-time computations and have manageable computing requirements. In practice, engineering implementation depends more on sensing and communication reliability, actuator saturation handling, and fail-safe design. Under extreme currents or sensor anomalies, redundant sensing and remote monitoring/takeover mechanisms are still required to ensure operational safety.

From a maritime safety-governance perspective, existing bridge-area protection systems mainly emphasize structural impact resistance and consequence mitigation. The proposed method shifts the handling window forward to the stage "after warning but before contact". It uses controllable thrust output to reduce the probability of hazardous approach, thereby complementing passive protection. This strategy provides an implementable pathway for proactive risk suppression in bridge areas. Its applicable scope and upper-bound benefits still need to be quantified and validated under more complex environments and constraints.

## 7. Conclusions

This paper investigates near-bridge collision risk associated with yaw deviation of vessels operating in inland bridge areas. We propose an active-intervention framework organized as an executable pipeline comprising state estimation and short-horizon prediction, yaw-deviation risk identification, push-assist decision making, and closed-loop corrective control. A discrete Kalman filter is employed to obtain fused estimates of planar motion states and to support short-horizon prediction. Risk entry due to yaw deviation is detected using threshold-based criteria combined with continuous decision logic. At the control layer, a thruster (push-thrust) model is incorporated, and an extended state observer (ESO) is used to estimate online the lumped effects of modeling uncertainties and

environmental disturbances. A fuzzy self-tuning incremental PID then generates thrust commands, enabling coordinated push–rudder closed-loop correction.

Within the bridge-area geometry and parameter ranges considered in this study, and under the assumption that a feasible handling window exists, numerical simulations and comparative tests indicate that push-assisted intervention can offer advantages over rudder-only recovery. Specifically, the proposed strategy tends to yield faster and more stable trajectory reconvergence, reduced accumulation of lateral deviation, and improved maintenance of safety margin in the vicinity of bridge piers. Under scenarios involving a constant cross-current disturbance, the combination of risk-triggered activation and ESO-based compensation produces relatively smooth thrust commands while preserving a stable recovery process. Overall, the results suggest that the proposed framework can serve as a practical engineering pathway to complement conventional "identification/early warning" schemes with actionable maneuvering intervention in bridge-area risk handling.

It should be emphasized that these findings are primarily supported by numerical validation under a limited set of operating conditions and should therefore be interpreted within that scope. More challenging and realistic conditions remain to be investigated, including strong crosswinds/strong cross-currents, shallow-water nonlinear hydrodynamics, and coupled effects of thrust saturation and actuator dynamics (e.g., delay and rate limits). Such factors may alter both closed-loop performance and the attainable improvement in safety margin. Future work will focus on systematic sensitivity and robustness studies across a broader range of vessel types, bridge geometries, and environmental conditions. In addition, the proposed method will be further verified and refined through higher-fidelity validation, including hardware-in-the-loop (HIL) experiments, scaled towing-tank tests, and, where available, full-scale operational data from bridge-area navigation, to strengthen engineering credibility and more clearly delineate the method's domain of applicability.

**Author Contributions:** Conceptualization, X.H. and L.H.; methodology, T.W.; software, Y.Z. and T.W.; validation, C.F., Y.Z. and L.H.; formal analysis, Y.Z.; investigation, C.F. and Y.Z.; resources, L.H.; data curation, C.F. and T.W.; writing—original draft preparation, Y.Z. and T.W.; writing—review and editing, C.F.; visualization, X.H.; supervision, L.H.; project administration, X.H.; funding acquisition, L.H. All authors have read and agreed to the published version of the manuscript.

**Funding:** This research was funded by the National Natural Science Foundation of China, grant number 52071248, the Research Program of Hubei Key Laboratory of Inland Shipping Technology, grant number NHHY2023004.

**Institutional Review Board Statement:** Not applicable.

**Informed Consent Statement:** Not applicable.

**Data Availability Statement:** The original contributions presented in this study are included in the article. Further inquiries can be directed to the corresponding author.

**Conflicts of Interest:** The authors declare no conflicts of interest.

## References

1. Chen, J.; Wei, X.; Huang, J.; Wang, H.; Dai, M. Research on High-Pressure Water Jet Interference for Collision Prevention of Waterway Viaduct Piers: Case Study of Guangzhou Lixin sha Bridge. *Buildings* **2024**, *14*, 2118. [CrossRef]
2. Pan, J.; Wang, Y.; Wang, T.; Xu, M. Study on Assessment of Collision Probability between Ship and Bridge Based on Automatic Identify System Data. *J. Mar. Sci. Eng.* **2024**, *12*, 452. [CrossRef]
3. Zhang, W.Z.; Pan, J.; Sanchez, J.C.; Bin Li, X.; Xu, M.C. Review on the Protective Technologies of Bridge against Vessel Collision. *Thin-Walled Struct.* **2024**, *201*, 112013. [CrossRef]

4. Dai, L.; Fang, H.; Wang, R.; Zhu, L.; Yao, P. Experimental Study and Numerical Simulation of Bridge Steel Pipe Pile Cofferdam Anti-Collision with Energy-Absorbing Lightweight Aggregate Filling. *Eng. Mech.* 2024. *in press*. Available online: https://kns.cnki.net/KCMS/detail/detail.aspx?dbcode=CAPJ&dbname=CAPJLAST&filename=GCLX20240412005 (accessed on 30 December 2025). (In Chinese)
5. Zhang, G.; Liu, Y.; Liu, J.; Lan, S.; Yang, J. Causes and Statistical Characteristics of Bridge Failures: A Review. *J. Traffic Transp. Eng. (Engl. Ed.)* **2022**, *9*, 388–406. [CrossRef]
6. Knott, M.; Winters, M. Ship and Barge Collisions with Bridges over Navigable Waterways. 2018. Available online: https://www.semanticscholar.org/paper/SHIP-AND-BARGE-COLLISIONS-WITH-BRIDGES-OVER-Knott-Winters/17835fb7e9b809f641e4769fe8292a53f7903d6a (accessed on 2 January 2026).
7. Bridge Risk (Johns Hopkins University). Available online: https://bridgerisk.engineering.jhu.edu/ (accessed on 31 December 2025).
8. Fan, W.; Zhong, Z.W.; Wang, J.J.; Xia, H.; Wu, H.; Wu, Q.L.; Liu, B. Vessel–Bridge Collisions: Accidents, Analysis, and Protection. *China J. Highw. Transp.* **2024**, *37*, 38–66. [CrossRef]
9. Fang, H.; Ju, W.; Zhu, L.; Zhang, X.C.; Yao, P.F. Ship Collision Test and Simulation of Bridge Steel Pipe Pile Cofferdam Filled with Sand Particles. *China J. Highw. Transp.* **2024**, *37*, 83–95. (In Chinese) [CrossRef]
10. Liu, K.; Zhang, Z.; Wang, J.; Yu, T.Q. Damage Characteristics of a Novel Vessel–Bridge Collision Protection Device Based on Trapezoidal Aluminum Foam Composite Sandwich Structure. *Ship Mech.* **2025**, *29*, 629–644. (In Chinese)
11. Chen, K. Low-Velocity Impact Performance of Steel Trapezoidal Corrugated (Hybrid) Sandwich Panels. Master's Thesis, Huazhong University of Science and Technology, Wuhan, China, 2019. Available online: https://kns.cnki.net/KCMS/detail/detail.aspx?dbcode=CMFD&dbname=CMFD201901&filename=1018802627.nh (accessed on 31 December 2025). (In Chinese)
12. Liang, Y.; Cui, P.; Fu, H. Research on an Intelligent Active–Passive Anti-Collision Early-Warning System for Waterway Bridges. *Traffic Energy Sav. Environ. Prot.* **2024**, *20*, 213–217. (In Chinese)
13. Xuan, X.; Yang, B.; Pan, J.; Wang, H.W.; Li, H.M. Application of a Multi-Bridge-Linked Active Early-Warning System for Bridge Anti-Ship Collision in Inland River Basins. *Port Waterw. Eng.* **2025**, *62*, 36–40. (In Chinese) [CrossRef]
14. Xu, S.; Liu, G.; Wang, J. Study on an Active Anti-Collision Early-Warning System for Bridges under Restricted Navigation Space. *Low Carbon World* **2025**, *15*, 169–171. (In Chinese) [CrossRef]
15. Hörteborn, A.; Ringsberg, J.W.; Lundbäck, O.; Mao, W. Probabilistic analysis of ship-bridge allisions when designing bridges. *Reliab. Eng. Syst. Saf.* **2025**, *260*, 111026. [CrossRef]
16. Wang, X.; Zheng, Z.; You, J.; Qin, Y.; Xia, W.; Zhou, Y. BOPVis: Bridge Monitoring Data Visualization for Operational Performance Mining. *Appl. Sci.* **2024**, *14*, 6615. [CrossRef]
17. American Association of State Highway and Transportation Officials (AASHTO). *Guide Specification and Commentary for Vessel Collision Design of Highway Bridges*; AASHTO: Washington, DC, USA, 1991.
18. Frangopol, D.M.; Dong, Y.; Sabatino, S. Bridge Life-Cycle Performance and Cost: Analysis, Prediction, Optimisation and Decision-Making. *Struct. Infrastruct. Eng.* **2017**, *13*, 1239–1257. [CrossRef]
19. Perera, L.P.; Guedes Soares, C. Collision Risk Detection and Quantification in Ship Navigation with Integrated Bridge Systems. *Ocean Eng.* **2015**, *109*, 344–354. [CrossRef]
20. Hörteborn, A.; Ringsberg, J.W. A Method for Risk Analysis of Ship Collisions with Stationary Infrastructure Using AIS Data and a Ship Manoeuvring Simulator. *Ocean Eng.* **2021**, *235*, 109396. [CrossRef]
21. Wang, F.; Chang, H.J.; Ma, B.H.; Wang, Y.-G.; Yang, L.-M.; Liu, J.; Dong, X.-L. Flexible Guided Anti-Collision Device for Bridge Pier Protection against Ship Collision: Numerical Simulation and Ship Collision Field Test. *Ocean Eng.* **2023**, *271*, 113696. [CrossRef]
22. Wang, H.; Wang, L.; Huang, Y.; Chen, X.; Yang, Y.; Zhou, Y.; Wei, F.; Wu, L.; Yang, J. Active Ship Collision Prevention Early Warning and Intercepting Device for Bridge. China Utility Model Patent CN220709791U, 2 April 2024. Application No. 202322145554.8. (In Chinese)
23. Park, J.-S.; Nguyen, T.-N.; Dinh, C.-T.; Huynh, T.; Kim, Y.-B. Modeling and Control of Tugboat-Assisted Operation for Marine Vessels. *J. Mar. Sci. Eng.* **2025**, *13*, 804. [CrossRef]
24. Luo, X.; Wang, J.; Li, J.; Lu, H.; Lai, Q.; Zhu, X. Research on Ship Trajectory Prediction Using Extended Kalman Filter and Least-Squares Support Vector Regression Based on AIS Data. In *Proceedings of the 2021 6th International Conference on Intelligent Transportation Engineering (ICITE 2021), Beijing, China, 29-31 October 2021*; Zhang, Z., Ed.; Lecture Notes in Electrical Engineering; Springer: Singapore, 2022; Volume 901, pp. 1123–1131. [CrossRef]
25. Zhang, H.; Zhang, X.; Bu, R. Active Disturbance Rejection Control of Ship Course Keeping Based on Nonlinear Feedback and ZOH Component. *Ocean Eng.* **2021**, *233*, 109136. [CrossRef]
26. Zhang, T.; Liao, Y.; Yang, C.; Wan, L.; Wei, T. Design of Data-Driven Extended State Observer for USV Heading Control Based on Dynamic Linearization. *Ocean Eng.* **2025**, *332*, 121426. [CrossRef]
27. Pérez-Pérez, E.J.; Puig, V.; López-Estrada, F.R.; Valencia-Palomo, G.; Santos-Ruiz, I. Neuro-fuzzy Takagi–Sugeno observer for fault diagnosis in wind turbines. *IFAC-PapersOnLine* **2023**, *56*, 3522–3527. [CrossRef]

28. Pérez-Pérez, E.J.; Puig, V.; López-Estrada, F.R.; Valencia-Palomo, G.; Santos-Ruiz, I.; Samada, S.E. Fault detection and isolation in wind turbines based on neuro-fuzzy qLPV zonotopic observers. *Mech. Syst. Signal Process.* **2023**, *191*, 110183. [CrossRef]
29. Fan, Y.; Qiao, S.; Wang, G.; Chen, S.; Zhang, H. A Modified Adaptive Kalman Filtering Method for Maneuvering Target Tracking of Unmanned Surface Vehicles. *Ocean Eng.* **2022**, *266*, 112890. [CrossRef]
30. Faragher, R. Understanding the Basis of the Kalman Filter via a Simple and Intuitive Derivation (Lecture Notes). *IEEE Signal Process. Mag.* **2012**, *29*, 128–132. [CrossRef]
31. Xu, T.; Cai, F.; Hu, Q.; Yang, C. AIS Trajectory Estimation of Ships Based on Kalman Filtering Algorithm. *Mod. Electron. Tech.* **2014**, *37*, 97–100+104. (In Chinese)
32. Welch, G.F. Kalman Filter. In *Computer Vision: A Reference Guide*; Ikeuchi, K., Ed.; Springer: Cham, Switzerland, 2021; pp. 721–723. [CrossRef]
33. He, Y.; Dai, Y.; Zhao, X.; Yu, D.Q.; Huang, Y.L. Navigation Decision Method for Waters with Variable Navigable Width in Estuary Deep Channel. *J. Shanghai Jiao Tong Univ.* **2025**, *59*, 489–502. (In Chinese)
34. Taniguchi, T.; Maki, A. A proposal of the maneuvering motion model for low-speed operations in harbor. *Ocean. Eng.* **2025**, *330*, 121172. [CrossRef]
35. Li, S.; Liu, C.; Chu, X.; Zheng, M.; Wang, Z.; Kan, J. Ship Maneuverability Modeling and Numerical Prediction Using CFD with Body Force Propeller. *Ocean Eng.* **2022**, *264*, 112454. [CrossRef]
36. Mikulec, M.; Piehl, H. Development of a modified body force method for modelling azimuth thrusters in CFD-based manoeuvring simulations. *Ocean. Eng.* **2025**, *319*, 120171. [CrossRef]
37. Xu, H.; Li, C.; Yu, W.; Han, S.M.; Wei, Y.F.; Yang, S.J. Intelligent Ship Track-Tracking Predictive Control Based on Extended State Observer. *J. South China Univ. Technol. (Nat. Sci.)* **2021**, *49*, 143–152. (In Chinese)
38. Mitsuyuki, T.; Kuribayashi, K.; Fernandez, R.F.S.; Shimozawa, H.; Kakuta, R.; Niki, R.; Matsushita, R. MMG 3DOF Model Identification with Uncertainty of Observation and Hydrodynamic Maneuvering Coefficients Using MCMC Method. *J. Mar. Sci. Technol.* **2024**, *29*, 668–682. [CrossRef]
39. Sang, H.; Zhou, Y.; Sun, X.; Yang, S. Heading Tracking Control with an Adaptive Hybrid Control for Under-Actuated Underwater Glider. *ISA Trans.* **2018**, *80*, 554–563. [CrossRef] [PubMed]
40. He, Y.; Xue, H.; Liu, X.; Xu, K.X.; Zhang, K.; Zhao, X.Y. Path-Tracking Method for Curved Channels Considering Non-Uniform Flow-Field Disturbances. *J. Shanghai Jiao Tong Univ.* **2025**. (In Chinese) [CrossRef]
41. Fossen, T.I. *Handbook of Marine Craft Hydrodynamics and Motion Control*; John Wiley & Sons: Chichester, UK, 2011.
42. Han, J. From PID to active disturbance rejection control. *IEEE Trans. Ind. Electron.* **2009**, *56*, 900–906. [CrossRef]


**Disclaimer/Publisher's Note:** The statements, opinions and data contained in all publications are solely those of the individual author(s) and contributor(s) and not of MDPI and/or the editor(s). MDPI and/or the editor(s) disclaim responsibility for any injury to people or property resulting from any ideas, methods, instructions or products referred to in the content.